

This document is the Accepted Manuscript version of a Published Work that appeared in final form in Corrosion Science., after peer review and technical editing by the publisher. To access the final edited and published work see <https://doi.org/10.1016/j.corsci.2023.111053>.

Novel Magnetron Sputtered Yttria Silica Iron Oxide as CMAS Resistant Top Coat material for Environmental Barrier Coatings.

Alexandra Rose, Juan T. Gomez-Chavez, , Peter Mechnich, Klemens Kelm, Uwe Schulz and Ravisankar Naraparaju*.

German Aerospace Center (DLR), Institute of Materials Research, Cologne, 51170, Germany

*Corresponding author

Email address: ravisankar.naraparaju@dlr.de (Ravisankar Naraparaju)

A nano-crystalline coating containing X2-yttrium monosilicate, yttrium ferrite and yttria was developed as a potential CaO-MgO-Al₂O₃-SiO₂ (CMAS) resistant top layer for Environmental Barrier Coatings (EBCs) to protect Ceramic Matrix Composites. High temperature reactions at 1300 °C with a synthetic CMAS and Colima volcanic ash revealed that the phases react quickly with the melt to oxyapatite and garnet which effectively restricted the infiltration into the coating. The Fe played a major role in stabilizing the multi-phase coating as well as X2-yttrium monosilicate. Iron-free YSi-Ox coatings could not induce garnet formation and found to be less effective in restricting the CMAS infiltration.

Keywords: Rare earth oxides, sputtered films, oxide coatings, CMAS

1. Introduction

Environmental barrier coatings (EBC) are used to protect materials such as SiC/SiC ceramic matrix composites (CMCs) against oxidation and recession due to water vapor in the hot part of aero-engines for aircrafts [1-4]. SiC oxidizes into SiO₂ and CO under high temperatures. Under water vapor environment (such as the gas turbine environment which contains steam), SiO₂ volatilizes into Si(OH)₄ leading to a quick recession of SiC [5-7]. EBCs must have a very low activity of SiO₂ (a_{SiO_2}) to reduce the SiC recession rates significantly [8]. Another most essential criteria for any EBC material is to match its coefficient of thermal expansion (CTE) to that of SiC-based CMCs ($\sim 4.5 \times 10^{-6} \text{ K}^{-1}$) to minimize the stress at the interface between the layers. Multi-layered rare earth (RE) mono- and disilicates, such as yttrium monosilicate Y₂SiO₅ (X2-YMS with $a_{SiO_2} \sim 0.33$ and CTE $\sim 7.7 \times 10^{-6} \text{ }^\circ\text{C}^{-1}$) and yttrium disilicate (γ -YDS with $a_{SiO_2} \sim 0.5$ and CTE $\sim 3.9 \times 10^{-6} \text{ }^\circ\text{C}^{-1}$) are applicable at temperatures up to 1500 °C and therefore preferred for EBC application [1-3, 8-11]. However, YMS exhibits two polymorphs, the low temperature X1-YMS and high temperature X2-YMS (above 1190°C) whereas YDS has 5 polymorphs with phase transformations between 1035-1535°C [12-14].

At higher temperatures, CMAS particles react with EBC materials and cause thermo-mechanical and thermo-chemical damages [9, 15-16]. It is generally proven that Y-containing ceramics show very good

reaction-crystallization ability in the reaction with CMAS, compared to structurally similar Yb- or Sc-silicates. It is understood that the RE^{3+} from the coating material dissolves into the molten CMAS/Volcanic ash (VA), leading to chemical reactions and formation of new crystalline products [15, 17-24] such as $Ca_2RE_8Si_6O_{26}$ (oxyapatites) or RE-containing garnet phases [9, 17, 22-25]. Progressive dissolution of the ceramic coating material into the molten CMAS leads to a fast coating recession. Poerschke et al. investigated the reactions between CMFAS and Atmospheric Plasma Spray (APS) YDS coatings on SiC/SiC CMCs at 1300 °C. The coating with a thickness of 275 μm dissolved into the CMFAS melt very quickly and was consumed within 24 h [10]. On the other hand, RE_2SiO_5 dissolves in the CMAS melt and was reported to form also apatite phase but consuming both CaO and SiO_2 , leading to continuous consumption of the CMAS melt. Therefore, the recession of the YDS-coating is faster compared to YMS [10]. Additionally, reactive crystallization generates tensile stresses, which in turn lead to crack formation upon engine cooling [16, 26-27]. It is well understood that the apatite phase is essential for sealing the coating and blocking further CMAS infiltration [28-30] however, this phase alone is not enough to mitigate the CMAS attack. Several studies by the authors showed that yttria rich TBC compositions have the capability to form both apatites and stable garnets which mitigate the CMAS attack more effectively [31-32]. Garnet formation consumes less amount of RE elements and more glass constituents in comparison to apatite formation. In another study, 65wt% Y_2O_3/ZrO_2 coatings showed an improved CMAS resistance at 1250 °C which was also traced back to the formation of stable Y-based apatite crystals [33]. Even though formation of a quick sealing apatite assures the blocking of inter-columnar gaps, garnet as a secondary product at the interface would crystallize the CMAS residue and stop the further growth of the reaction layer. Other own work revealed that a minimum of 8 at.% of FeO is needed to form a garnet phase as a reaction product of CMFAS and APS Y_2O_3 coatings [34]. Anticipating that both the high yttria and FeO effectively control the crystallization reactions with CMAS, a new Y_2SiO_5 - Y_2O_3 -FeO multi-phase coating (YSiFe-Ox) has been developed as a CMAS resistant layer as a topcoat for EBC applications [35-36] where YMS provides compatibility and a much lower CTE mismatch with the underlying YMS EBC layer. Yttria provides CMAS resistance and FeO promotes reactive crystallization within CMAS. An additional FeO-free YSi-Ox coating (having similar molar ratios of $YO_{1.5} : SiO_2$ to that of the YSiFe-Ox) was deposited employing magnetron sputtering. This paper presents the crystallization heat-treatment study and the corresponding evolution of multi-phase in the coating. The role of FeO on the phase stabilities of YMS at high temperature is additionally explored. High temperature interactions between CMAS/VA and the YSiFe-Ox/ YSi-Ox coatings were studied and the corresponding response is presented and discussed.

2. Material and methods

The YSiFe-Ox coatings were fabricated using a two-source magnetron sputtering facility (Systec SVS vacuum coatings, Germany). Coatings were produced by reactive magnetron sputtering using an yttrium-iron target power of 800 W and a silicon target power of 300 W under a chamber pressure of

4.4×10^{-3} mbar in Ar (flow rate of 23 sccm) and O_2 (flow rate of 6 sccm), with a substrate temperature of approx. 150 – 300 °C. The substrates were rotated with 10-12 rpm and coated with a sputtering rate of 3.8 $\mu\text{m}/\text{h}$. Initially, the coatings were produced on 1 mm thick alumina substrates to develop proper stoichiometry and sufficient thickness. After obtaining the desired coating chemistry, the same coatings were produced on 1.4 mm thick YMS pellets.

Most experiments were carried out on alumina substrates such as heat-treatments, phase analyses, etc., but compatibility with YMS and the role of surface roughness that will be present on a CMC was checked additionally with selected “more realistic” experiments on YMS pellets. The YMS pellets were produced by an aqueous solution that was prepared of $Y(\text{NO}_3)_3 \cdot x\text{H}_2\text{O}$ ($c=1$ mol/L) and nanosized fumed silica (Manufacturer: Aerosil) ($c=0.5$ mol/L) to achieve a ratio of 2:1. The suspension was homogenized for a few minutes by e.g. using the ultrasonic treatment and afterwards dried at temperatures up to 400 °C. The dried product was crushed in a mortar, and pellets were pressed in a mould (1 cm diameter, 1.4 mm thickness) and sintered afterwards at 1650 °C for 2 h.

Crystallization heat-treatments was carried out in a pre-heated thermal cyclic furnace, where the as-coated specimen was moved into and heated quickly to 1250 °C, followed by isothermal holding in air for 1 h at 1250 °C and then air quenched to RT with fans.

The selected CMAS/VA source for infiltration experiments had a composition of 48.1SiO₂-35.3CaO-9.6MgO-7.0Al₂O₃ (mol.% as produced by studies performed at the University of California Santa Barbara UCSB, therefore named “UCSB CMAS” further on), and the natural volcanic ash corresponding to the Colima volcano located in central Mexico (named Colima VA) and has a composition of 77.4SiO₂-5.6CaO-0.3MgO-4.3Al₂O₃-3.6FeO-0.8TiO₂-7.9Na₂O-0.1K₂O in mol.% [37-39]. The selection of these CMAS/VA compositions was based on the fact that they represent either CaO or SiO₂ rich mixtures so that the CMAS resistance of the developed coatings would be tested for a broad range.

Infiltration experiments were carried out by depositing CMAS on top of the coated samples in the amount of 10 mg/cm² followed by isothermal heating for 1 h, and for selected coatings additionally for 5h at 1300 °C in a chamber furnace (heating/cooling rate: 10 K/min). Standard metallographic techniques were used for sample preparation for cross-section analysis. Scanning electron microscopy (SEM) (Ultra 55, Carl Zeiss NTS Germany, equipped with energy-dispersive spectroscopy (EDS) system (Aztec, Oxford Instruments, UK) was used to study and characterize the reacted zones and infiltration depths. Selected reaction interfaces were prepared for transmission electron microscopy (TEM) via focused ion beam sectioning (FIB) in a FEI Helios Nanolab 600i dual-beam system. The reaction products and the phases of the YSiFe-Ox coating were characterized by TEM (Tecnai F30, STEM, Philips, the Netherlands) with a windowless Apollo EDS detector (EDAX, USA). Qualitative XRD analysis was

also used for phase identification (Siemens D5000 diffractometer with a secondary graphite monochromator using CuK α radiation and Bruker Eva software). Phase quantification was done for selected samples by Rietveld refinement (D8-Advance diffractometer with XE-T detector using CuK α radiation and Topas software, all Bruker AXS).

3. Results

3.1 Crystallization heat-treatment and corresponding microstructure of the YSiFe-Ox and YSi-Ox coatings

Coatings on alumina substrates

Fig. 1(a) & (b) show the cross-sectional SEM micrographs of the as-deposited, X-ray amorphous YSiFe-Ox and YSi-Ox coatings on Al₂O₃ substrates. As previously mentioned, alumina substrates were used during the initial stage of development. The YSiFe-Ox coating exhibited a dense but non-uniform microstructure having a thickness of ~ 19 μ m. The characteristic columnar growth pattern, caused by the sputtering process, with good adhesion of the coating to the alumina substrates was observed. The EDS measurements presented in Tab. 1 show that the coating exhibits inhomogeneities in the composition with YO_{1.5}: SiO₂ molar ratios between 2.25:1 (point 1 in Fig. 1) and 5.5:1 (point 2 in Fig. 1), where the molar ratio of YMS (3:1) lies in between. The additional FeO content varies between approx. 8 and 10 mol%. The YSi-Ox coating has ~26 μ m thickness and also shows good adhesion to the alumina substrate and exhibited a uniform, dense microstructure having small pores in the upper part of the coating (Fig.1 (b)). Similarly, the measured molar ratios of YO_{1.5}: SiO₂ in YSi-Ox coatings were measured as 3.4:1 and the composition was found to be uniform throughout the coating. The microstructure of as-coated YSi-Ox was found to be dense as shown in Fig. 1(b) and exhibited characteristic columns of a PVD method.

Fig. 1(c) show the YSiFe-Ox coating microstructure after the heat-treatment. The coating possesses an overall porosity of approximately 17 % (measured using Image J software), consisting of small pores pervading the whole coating. The coating thickness increased from 19 μ m (as-coated) to approx. 26 μ m. It stayed intact, but the columnar microstructure disappeared and exhibited small horizontal cracks and pores.

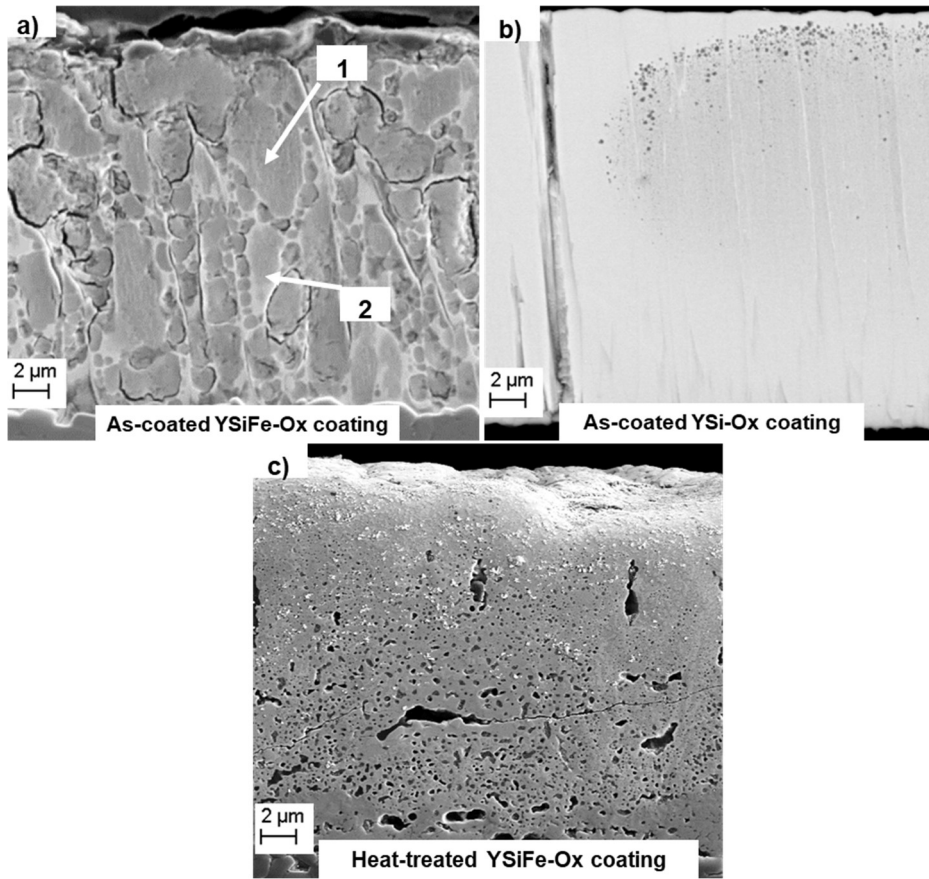


Figure 1: SEM cross-sections of (a) as coated YSiFe-Ox and (b) YSi-Ox and (c) heat-treated YSiFe-Ox coating on alumina.

Table 1: EDS analysis with resultant oxide quotients of the coating in as-coated condition of the heat-treated YSiFe-Ox and YSi-Ox coating.

As-coated YSiFe-Ox coating – EDS (Oxides in wt.%)			
Position	YO _{1.5}	SiO ₂	FeO
1	62	27.5	8.5
2	77	14	10
As-coated YSi-Ox coating -EDS (Oxides in wt.%)			
	YO _{1.5}	SiO ₂	
	77.3	22.7	

Table 2: Rietveld analysis of the heat-treated YSiFe-Ox and YSi-Ox coating.

Heat-treated YSiFe-Ox coating – Rietveld (wt.%)			
YFeO ₃	Y ₂ O ₃	X2-YMS	X1-YMS
23.7	22.4	53.9	-

Heat-treated YSi-Ox coating – Rietveld (wt.%)			
-	Y ₂ O ₃	X2-YMS	X1-YMS
-	57.5	5.9	36.6

Fig. 2 shows the XRD pattern of the 1250 °C heat-treated coatings in the 2 θ -range of 27–35°. YMS, Y₂O₃ and YFeO₃ reflections were identified. The very high-intensity peak at 29.5° can be assigned to yttria. The peak sequence (intensities and number of reflections) between 32–35° indicates the presence of the high temperature X2-YMS polymorph. This indicates that the heat-treatment favours the formation of the X2-YMS phase. YMS covers more than 50 % of the coating composition after the heat-treatment, according to Rietveld analysis (Table 2).

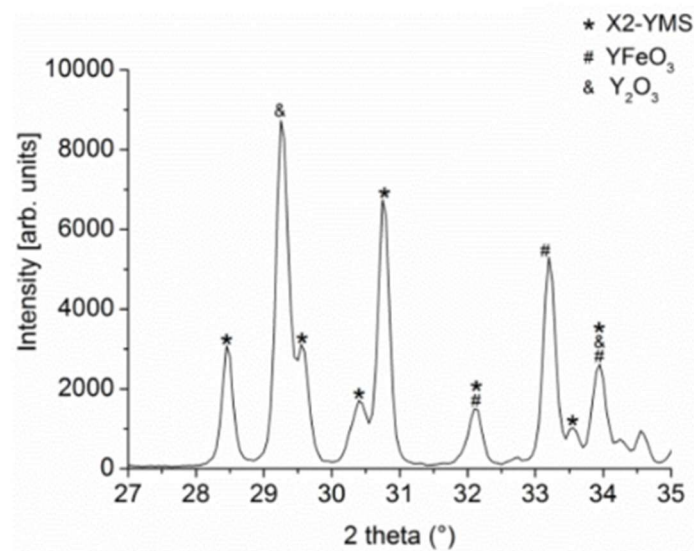


Figure 2: XRD pattern and peak assignment of the YSiFe-Ox coating in the 2 θ -range of 27–35° after heat-treatment.

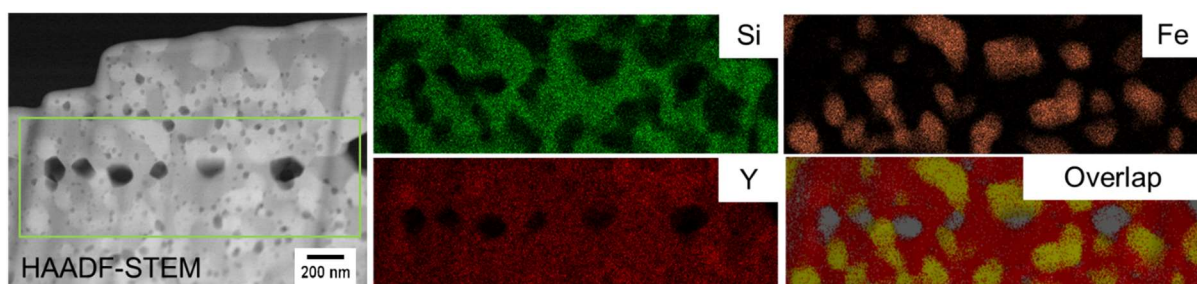


Figure 3: TEM EDS phase maps of YSiFe-Ox coating after heat treatment.

TEM was applied to analyse the distribution of YMS, Y₂O₃ and YFeO₃ phases in the coating and Fig. 3 shows the corresponding EDS elemental mapping of Y, Si and Fe. It can be clearly seen that yttria, silica and Fe rich nanograins are present and distributed uniformly within the coating. Electron-Diffraction was not successful due to their small size. However, their corresponding composition matches with XRD results shown in Fig. 2.

The same heat-treatments have resulted in entirely different scenarios for YSi-Ox coatings. The coatings on alumina substrates were peeled off during the heat-treatment. This could be due to the phase transition between low temperature X1-YMS and high temperature X2-YMS phases. The coating before and after the heat-treatment appears to be very dense. Thus, in the YSi-Ox coating the presence of multiple phases can lead to internal stresses in the coating. These stresses could arise from CTE mismatch of the multiple phases present in the coating or due to the crystal lattice volume changes of the YMS phases. Consequently, this volume change could have caused cracks and spallation of the ceramic top coat. (The X1-X2 YMS phase transformation and resulting volume change is considered as major reason for coating spallation of the YSi-Ox coating on alumina, because the CTE mismatch is quite small between alumina (CTE: $9.1 \cdot 10^{-6}/\text{K}$ for YSi-Ox and $9.6 \cdot 10^{-6}/\text{K}$ for Al_2O_3).

Coatings on YMS pellets

YMS pellets were porous and had a rough surface, which made it more difficult in determining a precise coating thickness. The coatings have undergone the crystallization heat-treatment and stayed intact to the substrates. The thickness of the YSiFe-Ox coatings was measured as $\sim 25\text{-}30 \mu\text{m}$. Due to the rougher surface of the YMS pellets, the coatings were not plane parallel to the surface, unlike that of alumina substrates. As a result, the coating surface possesses a wavy nature with notable microstructural changes compared to that on alumina substrates. The coating thickness has increased approximately by $10 \mu\text{m}$ after the heat-treatment and exhibited $\sim 16\%$ closed porosity. The microstructure exhibited smaller pores at the root zone, which follow a vertical line of the growth pattern forming a ‘teeth’ like structures mainly at the upper part of the coating, as shown in Fig. 4 (a).

A separation in darker and brighter areas, most likely between interior and column rim were found and this might correspond to phase separation and differences in composition. Longer annealing times such as 5h (not shown here) at this temperature gave rise to a more homogeneous and less columnar structure.

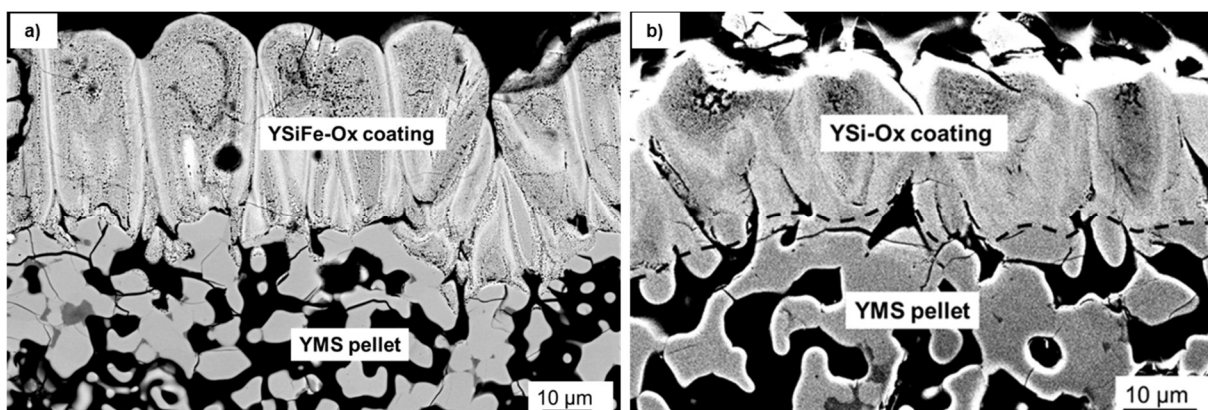


Figure 4: Cross-sectional BSE image of (a) YSiFe-Ox and (b) YSi-Ox coatings after heat-treatment.

In contrast to the alumina substrates, YSi-Ox coatings on YMS pellets were intact after heat-treatment and the formed phases were quantified by using the Rietveld method (Table 2). YSi-Ox coating

exhibited 57.5% yttria, and both X2 and X1-YMS phases comprised the rest, i.e. no single high temperature stable X2-YMS could be stabilized in the coating after the heat-treatment.

20-30 μm thick YSi oxide can be seen on YMS pellet after the heat-treatment shown in Fig. 4(b). The highly porous pellet provided a surface roughness that caused a highly inconsistent non-uniform coating. The coating exhibited a 'teeth' like structure similar to that of YSiFe-Ox coating, nonetheless experienced less closer porosity. From Table 2 it can be seen that YSi-Ox exhibited yttria rich and both X1 and X2 YMS phases after the heat-treatment. The YSi-Ox coatings exhibited a separation between Y-rich (bright) and YMS (dark) phases at the interior of the columns. Moreover, the yttria rich phase that was more situated at the column rims was found to be pore-free, whereas the YMS phase exhibited a porous microstructure.

3.2 CMAS/VA infiltration behaviour

YSiFe-Ox coatings deposited on Alumina substrates

Fig. 5a and b show SEM cross-sections of the UCSB CMAS exposed YSiFe-Ox coatings at 1300°C after 1h. A continuous 2-3 μm thick reaction layer consisting of small (0.5-1 μm) Y-Ca-oxapatite (A) crystals, protruding into the glass (#), was formed at the coating-glass interface. A few apatite crystals were also found to be dispersed in the glass. Selected area electron diffraction (SAED) performed in TEM confirmed the presence of hexagonal apatite, as shown in Fig 5e. Additionally, large garnet (G) crystals (7-12 μm diameter) were formed almost continuously at the reaction front as well as in the glass. The cubic garnet crystal structure was confirmed by SAED, too (see Fig. 5c). The elemental maps acquired in TEM-EDS (see Fig. 5f, h) show the enrichment of Fe and Y in the garnet grains.

G	10.6	11.6	37.5	26.6	3.7	10.0	garnet	garnet
A	-	-	39.3	13.7	-	47.0	apatite	apatite

Fig. 6a and b show the SEM cross-sections of the Colima VA exposed YSiFe-Ox coatings at 1300°C for 1h. A continuous 1-4 μm thick reaction layer consisting of small Y-Ca-oxyapatite (A) crystals, protruding into the glass (#), was formed at the coating-glass interface. SAED confirmed the presence of hexagonal apatite, as shown in Fig. 6e. Additionally, large YDS (D) crystals were found in SEM-EDS analysis (Fig. 6a). However, they could not be found in TEM analysis that could be due to its rare presence. Garnet (G) crystals were formed on top of the apatite. The cubic garnet crystal structure was confirmed by SAED, too (see Fig. 6c). The elemental maps by TEM-EDS (see Fig. 6f, h) also show the enrichment of Y and Fe in the garnet grains. It can be seen that barely any coating was consumed after VA exposure for 1 h. The presence of garnet fringe on top of the small apatite crystals (Fig. 6d) suggests that the garnet phase nucleates and grows at the expense of apatite, as suggested elsewhere [12, 30].

It is assumed that apatite forms as initial reaction product which forms on top of the coating as well as in the CMAS residue. In a later stage the apatite crystals from the CMAS residue slowly dissolve and forms garnet around the apatite crystals, by taking elements from the melt. This leads to the crystallisation of the melt. In addition, garnet also form directly at the coating/CMAS interface due to the diffusion of Fe from the coating to the reaction front. It appears that two different reactions kinetics are responsible for the garnet formation. This needs to be further investigated.

From the Ca elemental map (see Fig. 6i), it is evident that most of the molten VA was arrested by the continuous apatite layer, as described previously for the YSiFe-Ox coating exposed to UCSB CMAS. The elemental concentrations measured by TEM-EDS are summarised in Table 4.

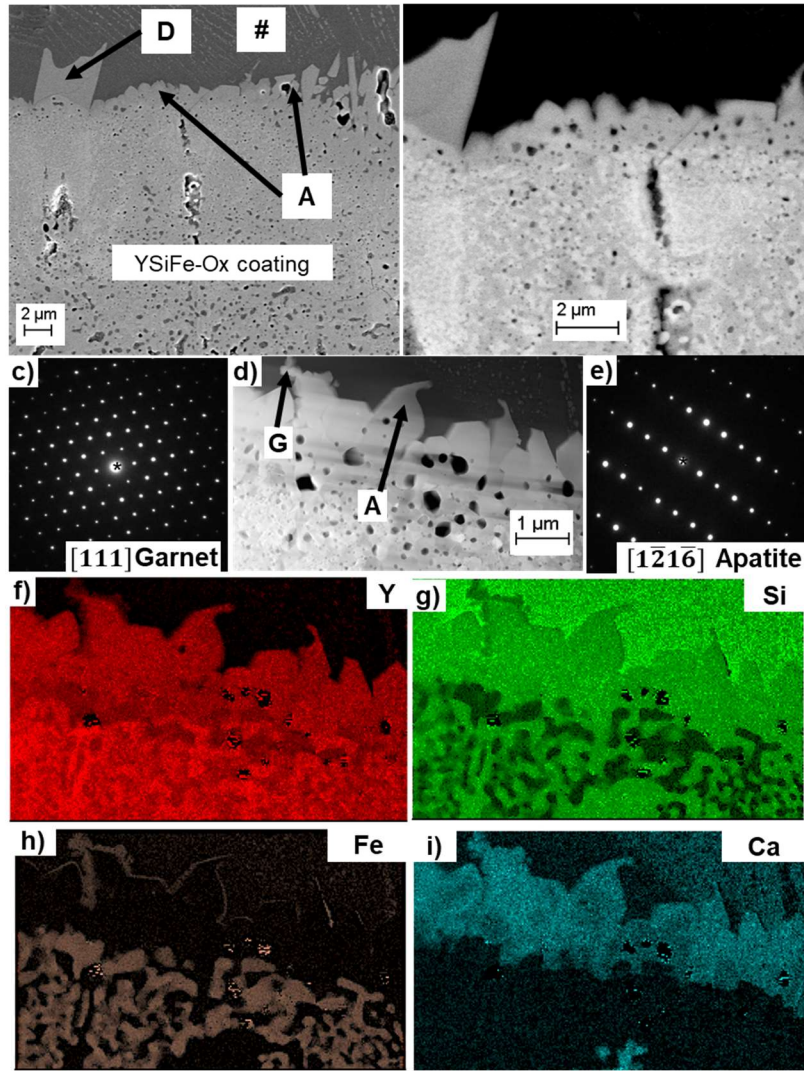


Figure 6: a) Cross-sectional SEM images of Colima VA interactions with the heat-treated YSiFe-Ox coating at 1300 °C for 1 h b) reaction front in high magnifications, c) SAED pattern of Garnet taken at G in Fig. 6d, d) HAADF-STEM image of Colima VA interactions with the heat-treated YSiFe-Ox coating at 1300 °C for 1 h, e) SAED pattern of apatite taken at A in Fig. 6d, c) elemental TEM-EDS mappings of f) yttrium, g) silicon, h) iron, i) calcium. A=apatite, G=garnet, D=YDS, #=glass

Table 4: Chemical composition of apatite and garnet phases from TEM/EDS measurements. Factory K-Factors were used from EDAX TEAM software. Although these may cause systematic errors, the compositions fall within the expected compositional range of the indicated phases. Infiltrated with Colima VA.

	Elemental composition at. %									Assumed phase from TEM EDS results	Confirmed phase by electron diffraction
	Na	Mg	Al	Si	K	Ca	Fe	Ti	Y		
G	0.9	7.7	8.7	21.3	0.4	10.8	25.4	1.4	23.4	garnet	garnet
A	-	-	-	39.8	-	10.7	-	-	49.4	apatite	apatite

YSiFe-Ox coatings deposited on YMS substrates

CMAS/VA infiltration experiments were additionally carried out between 1 and 5h at 1300°C to determine the coating consumption and reaction layer growth with respect to time and verify the compatibility with the underlying YMS pellet over time.

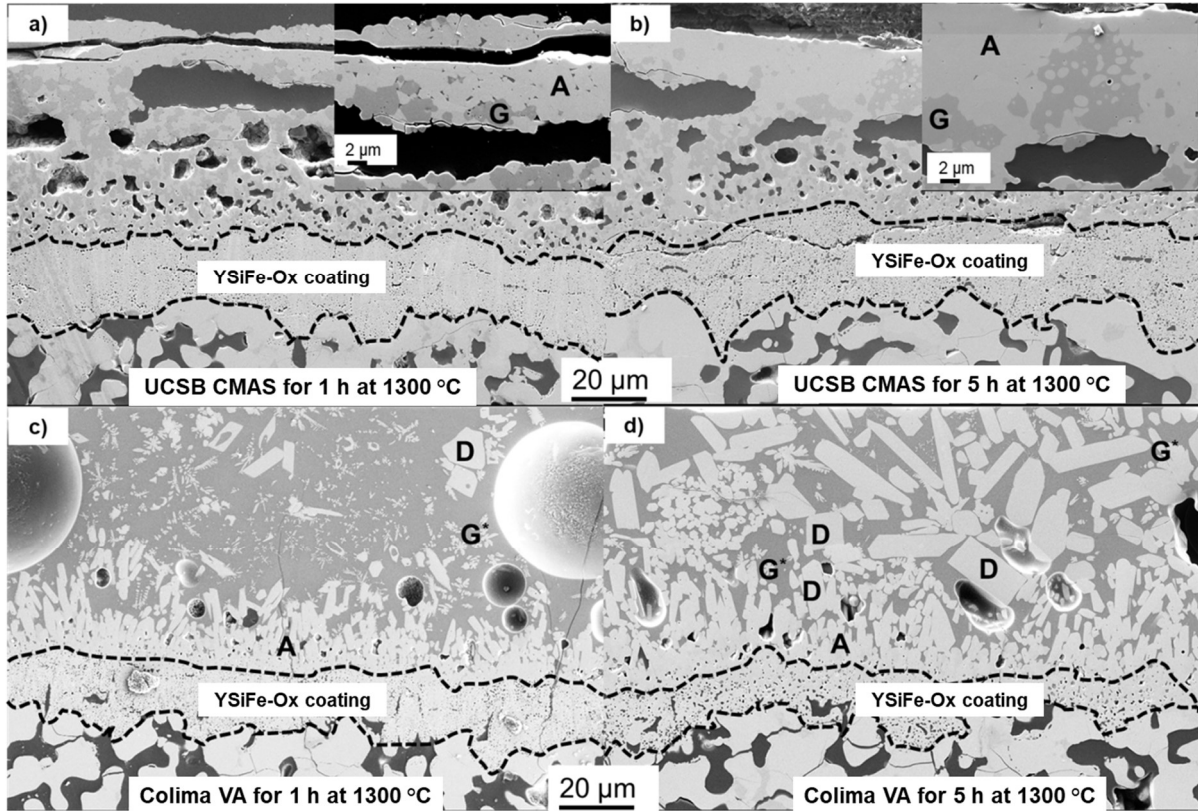


Figure 7: Cross-sectional SEM images of CMAS/VA interactions with the heat-treated YSiFe-Ox coating on YMS at a) UCSB CMAS for 1 h at 1300 °C b) UCSB CMAS for 5 h at 1300 °C c) Colima VA for 1 h at 1300 °C d) Colima VA for 5 h at 1300 °C. A=apatite, G=garnet, G*=dendritic garnet, D=YDS

Table 5: Chemical composition of reaction products of YSiFe-Ox coating and CMAS/VA infiltrated at 1300°C.

	Elemental composition at. %								Assumed phase from SEM-EDS results	Exposure time
	K	Na	Mg	Al	Si	Ca	Fe	Y		
A	-	-	-	-	41.7	9.0	-	49.3	apatite	Colima VA 1 h
G	0.5	2.4	3.8	9.7	33.0	7.0	13.5	30.1	garnet	Colima VA 1 h
A	-	-	-	-	39.7	8.5	-	51.8	apatite	Colima VA 5 h
G	0.7	3.3	3.9	16.5	24.3	5.2	23.9	22.2	garnet	Colima VA 5 h
D	-	-	-	-	48.5	-	-	51.5	YDS	Colima VA 5 h
A	-	-	-	-	38.4	14.1	-	47.5	apatite	UCSB CMAS 1 h
G	-	-	10.9	10.1	28.8	17.2	13.5	19.4	garnet	UCSB CMAS 1 h
A	-	-	-	-	37.3	13.1	-	49.6	apatite	UCSB CMAS 5 h
G	-	-	8.5	10.6	27.3	15.3	14.0	24.4	garnet	UCSB CMAS 5 h

Fig. 7a and b show the SEM cross-sections of the UCSB CMAS exposed YSiFe-Ox coatings on YMS at 1300 °C for 1 h and 5 h, respectively. The YSiFe-Ox coating exhibited a homogeneous microstructure and was not fully infiltrated by CMAS. The un-infiltrated coating is marked between the dashed lines. It can be seen that approximately one-third of the coating was consumed (10 µm) after CMAS exposure for 1 h and even 5 h. A clear reaction layer is not identifiable, which is in contrast to the case of YSiFe-Ox coating on alumina substrate (Fig. 5a&b). The remaining glass on top of the coating has fully reacted/crystallized and is especially shown in high magnification in the inset. Dark garnet (G) crystals and brighter apatite (A) crystals were found as reaction products on top of the coating, which seem to have the ability to crystallize large volumes of glass by using small amounts of the coating material. No inter-diffusion of yttria from YMS pellet into the coating was observed, and the interface was found to be crack free. The corresponding SEM-EDS results for the reaction products and identification are shown in Table 5.

Fig. 7c and d show the SEM cross-sections of the Colima VA exposed YSiFe-Ox coatings at 1300 °C for 1 h and 5 h, respectively. The YSiFe-Ox coating seems to be intact and not entirely infiltrated by the volcanic ash, though more coating has been consumed compared to the UCSB CMAS case. Around 10-15 µm of the coating has been consumed after 1h, and the reaction has further proceeded by consuming 20-22 µm after 5h. A clear reaction front can be seen, which consists of apatite crystals at the reaction/coating interface, whereas few YDS (D) crystals were dispersed in the accumulated glass after 1h. Few garnet dendrites were also found within the VA glass. Apatite crystals seem to grow in size at the reaction interface after 5h, and more were found to be dispersed in the glass (Fig. 7d). Additionally, more large YDS (D) crystals were found in comparison to the 1h case. Comparably few dendritic garnets (G *) were formed in the glass.

YSi-Ox coatings on YMS pellets

Fig. 8a and b show the SEM cross-sections of the UCSB CMAS exposed YSi-Ox coatings for 1 h at 1300 °C in low and high magnification, respectively. A continuous 2-3 µm thick reaction layer consisting of small Y-Ca-oxyapatite (A) crystals were formed at the coating-glass interface. Many apatite crystals were also found to be dispersed in the glass. Only 12-22 µm of the coating was left after the infiltration. It can be seen that the coating was locally infiltrated through the yttria/YMS phase boundaries as well as the columnar gaps of the coating after CMAS exposure as the YMS pellet underneath the YSi-Ox coating has highly reacted with the infiltrated CMAS forming apatite crystals (as shown in Fig. 8(a) encircled by the white dotted lines). The YSi-Ox coating spalled at the upper part, probably due to increased stresses caused by the CMAS infiltration/stiffening. No garnet phase was found at the interface or within the glass.

Fig. 8c and d show the SEM cross-sections of the Colima VA exposed YSi-Ox coatings for 1 h at 1300 °C. Phase separation of yttria (brighter) and YMS (darker) was strongly evident in the coating. A continuous 3-4 μm thick reaction layer consisting of small Y-Ca-oxypatite (A) crystals has formed at the coating-glass interface, as shown in Fig. 8(d). It can be seen that the coating has been infiltrated after VA exposure, and no apatite crystals were found in the residual VA. The YMS pellet underneath the YSi-Ox coating has also reacted with infiltrated VA, supporting the assumption that the coating was entirely infiltrated (encircled by white dotted lines in Fig. 8 (c)). Neither YDS crystals nor the dendritic garnets were observed within the glass. The difference in the apatite composition that was formed in case of UCSB and Colima VA that was measured by EDS spot analysis is given in Table 6.

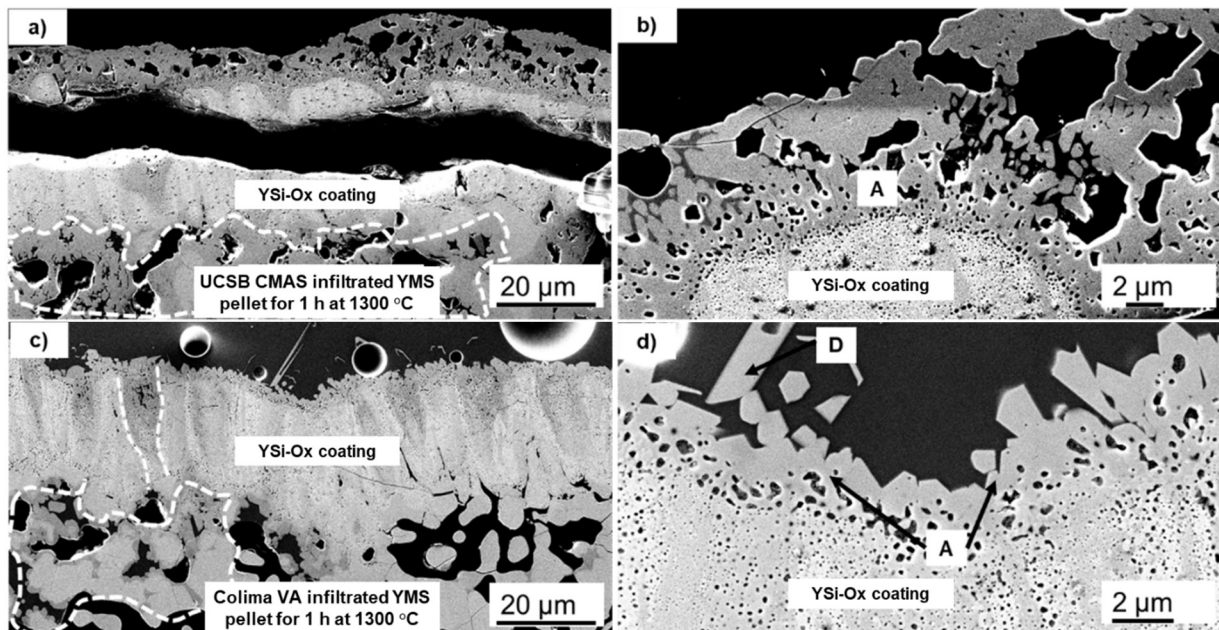


Figure 8: a) Cross-sectional SEM images of CMAS/VA interactions with the heat-treated YSi-Ox coating on YMS at a), (b) UCSB CMAS for 1 h at 1300 °C, (c)&(d) Colima VA for 1 h at 1300 °C.

Table 6: Chemical composition of apatite phase that formed due to the reaction of YSi-Ox coating and CMAS/VA infiltrated at 1300°C.

	Elemental composition at. %			Assumed phase from SEM-EDS results	Exposure time
	Si	Ca	Y		
A	36.7	16.4	45.9	apatite	UCSB 1 h
A	41	7.8	51.1	apatite	Colima VA 1 h

4 Discussion

A multi-phase nano-crystalline YSiFe-Ox coating was developed as a CMAS resistant top layer for EBCs. Generally, it is known that with the increase in the thickness of the apatite layer as a reaction product, the stiffness of the EBC increases, allowing crack formation and propagation, which ultimately leads to EBC failure. In that scenario, a thin coating must be sufficient to crystallize the CMAS, therefore the magnetron sputtering technique was used to produce 20-30 μm thick coatings in this study. Especially sputtering technique offers great control over the chemistry of non-stoichiometric compositions compared to plasma spray methods. Besides, the low thicknesses of the coating layers achieved by this method causes lower stresses and less cracking. For producing thicker coatings, other PVD methods such as Arc-PVD can be used. YSiFe-Ox was applied on top of the other thin film layers of an EBC system such as a silicon-based bond coat [40] and other silicate layers [41-42] and corresponding CMAS interactions are currently being studied and will be part of future publication. Based on the current findings, the topics that are discussed include (a) phase stabilization and microstructure of YSiFe-Ox coatings, (b) the mechanisms of reaction with high Ca/Si to low Ca/Si containing CMAS compositions and (c) the reactivity of iron-free YSi-Ox coatings with CMAS, as well as the influence of the substrate roughness on the infiltration behaviour.

4.1 Phase formation and the microstructure evolution during the crystallization heat-treatment

YSiFe-Ox

As-coated YSiFe-Ox exhibited a dense and columnar microstructure, as shown in Fig. 1(a) and a noticeable difference was observed in the microstructure after heat treatment. Uniformly distributed nano-crystalline Y_2O_3 , YFeO_3 and X2-YMS have evolved after the heat-treatment. It is known from the literature that YMS exhibits two polymorphs that undergo a transformation in the temperature range where current heat-treatments was carried out. This phase transformation leads to a volume change and causes stresses in the coating [43]. The observed pores in the current coating could have formed due to a quick X1-X2 YMS phase transformation and the formation of the other phases as the extent of diffusion process was low (see Fig. 1(c)). The coating appears to be quasi dense, which consisted of closed pores and, consequently, should be gas-tight. This kind of pores were also noticed in YMS coatings obtained by magnetron sputtering after heat treatment [13, 31]. It is believed that these pores compensate further thermal stresses due to lowering the Young's modulus, e.g. the volumetric changes in the lattice structure of YMS when it undergoes polymorphic transformations or in multi-layered coating system, that can lead to spallation of the coating [44-45]. It is believed that a multi-phase coating (composite coating) would generate micro-stresses due to their CTE mismatch upon thermal cycling, which ultimately can also lead to spallation. However, uniform distribution of nano-crystals of Y_2O_3 , YFeO_3 and X2-YMS, as shown in Fig.3, would exhibit lower local stress levels due to their smaller size. Based on the amount of each phase and their respective CTEs, an average CTE of YSiFe-Ox coating is

calculated as $6.9 \times 10^{-6}/K$ ¹, which corresponds to a mismatch of 0.9 ppm² with the underlying YMS pellet. Nonetheless, the lower thickness could compensate for the CTE mismatch and consequently no crack along the interface was observed in Fig.6. The behaviour of the new YSiFe-Ox coating on SiC-SiC CMC that possesses a much lower CTE is the topic of ongoing research.

As can be seen from the microstructure of the coatings on YMS pellets, there is still room for improvements in processing that would lead to more homogeneous coatings with optimized microstructure which is still the challenge of depositing PVD coatings on rough surfaces.

YSi-Ox

The as-coated YSi-Ox layer had a similar molar ratio of $YO_{1.5}$: SiO_2 than that of the YSiFe-Ox coating and exhibited an inhomogeneous microstructure as shown in Fig.4. This peculiar microstructure was previously observed by Leisner in his work on investigating YMS/YDS PVD coatings as EBCs [13]. Similar phase separation between column rim and interior of YMS with 10 mol% $YO_{1.5}$ excess was observed, after annealing treatment for 30 minutes at 1250 °C. At the column rim pure Y_2O_3 was found whereas at the interior a phase with Y/Si ratio of 2.5 was found. This could be explained by lack of oxygen in the interior coating, being not fully oxidized in an initial state, as in the column rims the oxygen diffusion is quicker causing an oxygen excess. This leads to RE-diffusion, in this case Y, to the top & column rims, due to the higher oxygen affinity of yttrium. Therefore, the Y oxide content at the column rims & near-surface areas is higher and differences in porosity appear [13]. This phenomenon and explanation can also be applied in our case of YSiFe/YSi-Ox coatings.

In addition to the microstructures, noticeable differences were observed in the phase constituents after the heat-treatment compared to YSiFe-Ox. No single high temperature stable X2-YMS phase was formed in the heat-treatment in the YSi-Ox coating. It implies the fact that there will always be phase transitions between X1-X2 during heating and cooling, which would generate volume change associated damage. This implies that the presence of FeO in the coating influences the stabilization of YMS polymorphs. It is known from the literature that FeO assists the kinetics of the reaction and favours the formation of equilibrium products in yttrium silicate mixtures [46]. FeO stabilizes the Y-Si-apatite phase above 1600°C and YMS and YDS below 1600°C. Based on the current results, it is hypothesized that FeO acts as a fundamental stabilizing agent for the formation of single-phase X2-YMS during the heat-treatment.

¹ Cumulative CTE values were calculated from the phase compositions obtained from Rietveld results with Y_2O_3 : $9.5 \times 10^{-6}/K$, X1-YMS: $8.7 \times 10^{-6}/K$, X2-YMS: $7.77 \times 10^{-6}/K$, $YFeO_3$ $2.28 \times 10^{-6}/K$.

² Mismatch calculated between YMS pellet ($7.77 \times 10^{-6}/K$) to YSiFe-Ox coating ($6.9 \times 10^{-6}/K$) with 1 ppm = $1 \times 10^{-6}/K$

Based on the Rietveld analysis shown in Table 2, the average CTE of the YSi-Ox coating was calculated as $9.1 \times 10^{-6}/\text{K}^3$ after heat-treatment, which implies a larger CTE mismatch with YMS and also with a CMC compared to YSiFe-Ox. Around 50% presence of pure yttria phase in any heat-treatment with almost no porosity can be advantageous concerning CMAS attack. However, the observed segregation of the YMS phase and Y-rich areas was proved to be detrimental to CMAS attack which is elaborated below.

4.2 Analysis of YSiFe-Ox coating reaction with siliceous melts

UCSB CMAS

Barely any coating was consumed after CMAS exposure for 1h, and a reaction layer consisting of small apatite crystals was formed at the coating/CMAS interface. Numerous large garnet crystals were formed in the residual CMAS as well as at the reaction interface. The Fe content found in the garnet confirms the Fe diffusion out of the coating, which can also be seen in the TEM elemental map in Fig. 5h. It has been observed previously that a high FeO content in CMAS tends to promote nucleation of the garnet phase [33]. This is in good agreement with findings by Eils et al. who showed in their studies that garnet could be formed in the reaction of iron-free UCSB-type CMAS with $\text{Y}_2\text{O}_3\text{-ZrO}_2$ and Y_2O_3 coatings fabricated by metal-organic chemical vapor deposition. However, they observed much less, isolated garnets, probably due to the absence of iron [30]. The presence of numerous and large garnets in this work confirms the diffusion of Fe from the coating and its governing influence for garnet formation. The additional presence of small apatite crystals within the larger garnets embedded in the residue (Fig. 7) suggests that the garnet phase can also nucleate and grow at the expense of apatite, as suggested elsewhere [19, 30]. From the Ca elemental map (see Fig. 5i), it is evident that the continuous apatite layer arrested most of the molten CMAS. Apatite's sealing nature was described previously in the literature and could be confirmed by this work [30]. Moreover, homogeneous distribution of nanocrystals of yttrium silicate and yttrium ferrite, besides an yttrium rich phase, controls the growth kinetics of apatite (see the small crystal size visible in Fig. 3), which reduces the recession rate of the coating. This indicates that apatite forms as an initial reaction product, while garnet is growing from the apatite accompanied by the incorporation of iron.

The apatite phase, is assumed to form as an immediate reaction product which consumes silica and calcia from the glass. On the other hand, apatite formation also consumes higher amounts of yttria from the coating that might lead to a faster coating recession, due to the continuous diffusion of Y^{3+} to the top of the coating and reaction with the glass as described elsewhere [18]. The apatite, which was found in the glass, exhibited a lower Y content compared to the apatite found at the reaction layer. However, it seemed that the Ca content decreased when the Y content increased, which leads to the assumption that Y and Ca are substitutable with each other in the apatite crystal structure, due to the similar ionic radii

³ Cumulative CTE values were calculated from the phase compositions obtained from Rietveld results with Y_2O_3 : $9.5 \times 10^{-6}/\text{K}$, X1-YMS: $8.7 \times 10^{-6}/\text{K}$, X2-YMS: $7.77 \times 10^{-6}/\text{K}$.

[47]. The observed apatite crystal sizes vary between $\sim 0.3 \mu\text{m}$ (at the reaction front) and $\sim 1 \mu\text{m}$ (in the glass) and were found to be similar to the results of Grant et al. [18]. The presence of 'floating' apatite crystals in the residual CMAS was also found in previous studies, however more obviously in the case of APS coatings but not in YMS/YDS pellets [10]. The residual CMAS glass was continuously infiltrating apatite grain boundaries facilitating the reaction to continue until the equilibrium is reached. Nevertheless, the garnet formation within the residue/reaction interface consumes much less yttria from the coating/apatite and takes all the glass components, leading to a reduced coating recession over time. The apatite formation continues until Fe from the coating diffuses into CMAS and starts the crystallization of garnet as a dominating reaction product. Besides the need for substantial Fe diffusion, the delayed garnet formation can also be explained by the higher stability of primary YFeO_3 as a potential Fe source for garnet formation. The main difference in the reaction behaviour of the YSiFe-Ox coating compared to YMS studies [10, 17-18] is the constant garnet formation, which leads to progressive melt consumption and reducing the Ca supply to the reacting interface, which suppresses the continuous apatite growth. This effect is supported by the size and shape of the apatite crystals, which otherwise grow into large needle-like prismatic crystals [10, 18]. The nearly dense tri-phase nanocrystalline coating assures the yttria supply (from the free yttria and YFeO_3 phase in the PVD coating) to the reaction front by suppressing the YMS dissolution and at the same time promotes the Fe diffusion for the crystallization of the glass. The Fe and Y diffusion to the top of the coating leads to a denser coating in the upper part (Fig. 5a). The low coating consumption also indicates that free Y_2O_3 in the coating was a preferred source for apatite formation than the YMS phase. A slight increase in the reaction layer depth was observed when YMS pellets were used ($\sim 10 \mu\text{m}$) instead of alumina ($2\text{-}3 \mu\text{m}$) as substrates even though no difference in the reaction products was observed. This change can be attributed to the non-uniform thickness of the coating and the 'teeth' like microstructure, which led to an uneven reaction front and more apatite crystals. No significant change in the thickness of the reaction layer was observed between 1 and 5h infiltration on both substrates, which assures the protective nature of the coating with time and a very sluggish progression of further coating recession.

Colima VA

The YSiFe-Ox coating on both alumina and YMS pellets produced the same reaction products after 1h at 1300°C . In both cases, YDS and dendritic garnets surrounding apatite crystals along with the continuous apatite reaction layer were observed (see Fig.6 & 7). The YDS crystals found at the reaction layer of the YSiFe-Ox coating were always observed on top of the continuous apatite layer, indicating the growth of YDS from apatite. The YDS formed probably due to the high Si content in the Colima VA. According to the Y-Si-O phase diagram, YDS forms if the Si content exceeds a Si:Y ratio of 0.5 [48]. Generally, the number of apatite crystals was reduced after 5 h of infiltration. In contrast, the amount of YDS crystals increased in the area of the reaction layer/residual CMAS, supporting the assumption that apatite converts in to YDS. The dendritic garnets, which were found with a small crystal fringe that was identified as garnet in TEM analysis as shown in Fig. 6, would have formed during

cooling. However, larger garnets were not found in the CMAS residue as in the case of UCSB CMAS. The limited amount of Ca availability in the melt was not sufficient for the extensive garnet formation. Considerable increase in the reaction layer thickness (~10 μm) from 1 to 5h infiltration time indicates that the coating/melt reaction continued by consuming the coating and forming new reaction products. It is hypothesized that the absence of larger garnet crystals as found in the case of UCSB CMAS, which crystallizes the melt residue and cut the Ca supply to the reaction front, is the main reason for this reaction layer growth with time.

4.3 Analysis of YSi-oxide coating reaction with siliceous melts

In comparison, YSi-Ox has formed only apatite at the reaction front for both the UCSB and Colima VA at 1300°C. No Garnet was found at the reaction front or in the residue glass in the case of UCSB CMAS which imposes the fact that FeO plays a major role in forming garnet. YDS crystal growth from apatite was also not observed in the case of YSiFe-Ox with Colima VA. The absence of YDS phase supports the finding of Parmentier et al. that iron promotes the apatite decomposition below 1600°C, as in the iron-free YSi-Ox coating apatite is present in large quantities after infiltration and did not decompose; i.e. Fe enforces the apatite decomposition into YDS and YMS, as well as formation of garnets as equilibrium reaction products [46]. However, the phase compositions of YSiFe-Ox and YSi-Ox coatings were not the same as shown in Tab. 1 that could have influenced the formation of reaction products as well, e.g. more Y^{3+} (50% yttria) is available in the YSi-Ox coating that can react with CMAS/VA. This led to a thin reaction layer at the interface (2-4 μm in both cases), which might be beneficial for CMAS resistance. However, the inhomogeneity in the YSi-Ox coating having inter-columnar gaps led to infiltration paths for molten CMAS/VA. Careful optimization of the Y_2O_3 +YMS region in terms of chemistry and proper heat-treatment to eliminate phase boundaries could be useful in terms of CMAS attack and is topic of ongoing research.

5 Conclusions

In summary, a novel magnetron sputtered multi-phase YSiFe-Ox coating was developed as a CMAS resistant coating for EBC applications on CMCs. A suitable heat-treatment consisting of rapid heating to 1250°C and 1h holding at 1250°C followed by air quenching to RT in lab air atmosphere was necessary to achieve the desired phases and microstructures. In order to study the role of iron in the new coating, a Fe-free YSi-Ox coating with similar molar ratio of $\text{YO}_{1.5}$: SiO_2 to the YSiFe-Ox coating was investigated and the same heat treatment was applied. Smooth alumina and rough YMS pellets were used as substrate materials. High temperature infiltration experiments with UCSB CMAS and Colima volcanic ash (VA) at 1250°C and 1300°C for different time intervals from 1h to 5h were performed to assess the performance of the coatings. Based on the obtained results following conclusions are drawn.

- 1) YSiFe-Ox exhibited uniformly distributed Y_2O_3 , YFeO_3 and X2-YMS nano phases with a nearly dense (closed porosity) but stress tolerant microstructure that does not crack.

- 2) YSi-Ox consisted of both X1 and X2 YMS in addition to the yttria phase. This suggests that FeO stabilises the high temperature non-transforming X2-YMS phase and more rapid heating/cooling favours the X2 phase.
- 3) Surface roughness of the substrate has played an important role in defining the final morphology of the developed coatings.
- 4) The YSiFe-Ox coating quickly reacted with high Ca/Si containing iron-free CMAS and a continuous thin apatite reaction layer was formed at the reaction front. Additional garnet crystals have formed at the reaction front as well as in the residue which prevented the continuous supply of Ca to the reaction front, which eventually slowed the coating recession down. The remaining YSiFe-Ox coating was quasi non-infiltrated, and no radical growth of the reaction layer was observed by prolonging the infiltration time from 1 to 5h at 1300°C. Fe diffusion into the melt played a significant role in the garnet formation.
- 5) The YSiFe-Ox coating also reacted quickly with low Ca/Si containing VA and formed apatite at the reaction front. However, due to the YDS formation and lack of garnet crystals in the residue, the continuous reaction layer growth was inevitable, and a recession in the coating with time has been observed.
- 6) The novel YSiFe-Ox coating offers great potential to be the CMAS resistant part of a multilayer EBC system to protect SiC-SiC CMCs.
- 7) In contrast, Fe-free YSi-Ox coatings have failed to assure the protection against CMAS infiltration mostly due to their inhomogeneity in phase distribution and presence of inter columnar gaps, which were vulnerable to the CMAS attack.

Acknowledgement

Authors would like to acknowledge Mr. Andreas Handwerk for producing coatings using magnetron sputtering. Authors would also like to acknowledge Dr. Leisner for his valuable input in the technical discussion in understanding the phase quotients of the coating system.

References

- [1] H.E. Eaton and G.D. Linsey, *Journal of the European Ceramic Society*, Accelerated oxidation of SiC CMC's by water vapor and protection via environmental barrier coating approach 22, 2741-2747 (2002). [https://doi.org/https://doi.org/10.1016/S0955-2219\(02\)00141-3](https://doi.org/https://doi.org/10.1016/S0955-2219(02)00141-3)
- [2] D. Zhu, *Aerospace Ceramic Materials: Thermal, Environmental Barrier Coatings and SiC/SiC Ceramic Matrix Composites For Turbine Engine Applications*, Glenn Research Center, 2018.
- [3] N.P. Padture, *Nature Materials*, Advanced structural ceramics in aerospace propulsion 15, 804-809 (2016). <https://doi.org/10.1038/nmat4687>
- [4] I. Spitsberg and J. Steibel, *International Journal of Applied Ceramic Technology*, Thermal and Environmental Barrier Coatings for SiC/SiC CMCs in Aircraft Engine Applications 1, 291-301 (2004). <https://doi.org/https://doi.org/10.1111/j.1744-7402.2004.tb00181.x>
- [5] K.N. Lee, D. Zhu and R.S. Lima, *Journal of Thermal Spray Technology*, Perspectives on Environmental Barrier Coatings (EBCs) Manufactured via Air Plasma Spray (APS) on Ceramic Matrix Composites (CMCs): A Tutorial Paper 30, 40-58 (2021). <https://doi.org/10.1007/s11666-021-01168-0>

- [6] E.J. Opila and R.E. Hann Jr, *Journal of the American Ceramic Society*, Paralineer Oxidation of CVD SiC in Water Vapor 80, 197-205 (1997). <https://doi.org/https://doi.org/10.1111/j.1151-2916.1997.tb02810.x>
- [7] E. Bakan, D.E. Mack, S. Lobe, D. Koch and R. Vaßen, *Journal of the European Ceramic Society*, An investigation on burner rig testing of environmental barrier coatings for aerospace applications 40, 6236-6240 (2020). <https://doi.org/https://doi.org/10.1016/j.jeurceramsoc.2020.06.016>
- [8] N.P. Padture, *npj Materials Degradation*, Environmental degradation of high-temperature protective coatings for ceramic-matrix composites in gas-turbine engines 3, 11 (2019). <https://doi.org/10.1038/s41529-019-0075-4>
- [9] K.N. Lee, A. Garg and W.D. Jennings, *Journal of the European Ceramic Society*, Effects of the chemistry of coating and substrate on the steam oxidation kinetics of environmental barrier coatings for ceramic matrix composites 41, 5675-5685 (2021). <https://doi.org/https://doi.org/10.1016/j.jeurceramsoc.2021.04.037>
- [10] D.L. Poerschke, J.H. Shaw, N. Verma, F.W. Zok and C.G. Levi, *Acta Materialia*, Interaction of yttrium disilicate environmental barrier coatings with calcium-magnesium-iron aluminosilicate melts 145, 451-461 (2018). <https://doi.org/https://doi.org/10.1016/j.actamat.2017.12.004>
- [11] E. Garcia, O. Sotelo-Mazon, C.A. Poblano-Salas, G. Trapaga and S. Sampath, *Ceramics International*, Characterization of Yb₂Si₂O₇-Yb₂SiO₅ composite environmental barrier coatings resultant from in situ plasma spray processing 46, 21328-21335 (2020). <https://doi.org/https://doi.org/10.1016/j.ceramint.2020.05.228>
- [12] Z. Sun, M. Li and Y. Zhou, *International Materials Reviews*, Recent progress on synthesis, multi-scale structure, and properties of Y-Si-O oxides 59, 357-383 (2014). <https://doi.org/10.1179/1743280414Y.0000000033>
- [13] V. Leisner, K. Kelm and U. Schulz, *Journal of the European Ceramic Society*, Thin single-phase yttrium-based environmental barrier coating systems for SiC/SiC CMCs 42, 7275-7287 (2022). <https://doi.org/https://doi.org/10.1016/j.jeurceramsoc.2022.08.035>
- [14] J.W. Nowok, J.P. Kay and R.J. Kulas, *Journal of Materials Research*, Thermal expansion and high-temperature phase transformation of the yttrium silicate Y₂SiO₅ 16, 22 (2001). <https://doi.org/10.1557/JMR.2001.0309>
- [15] K.M. Grant, S. Krämer, J.P.A. Löfvander and C.G. Levi, *Surface and Coatings Technology*, CMAS degradation of environmental barrier coatings 202, 653-657 (2007). <https://doi.org/https://doi.org/10.1016/j.surfcoat.2007.06.045>
- [16] B.J. Harder, J. Ramirez-Rico, J.D. Almer, K.N. Lee and K.T. Faber, *Journal of the American Ceramic Society*, Chemical and Mechanical Consequences of Environmental Barrier Coating Exposure to Calcium-Magnesium-Aluminosilicate 94, s178-s185 (2011). <https://doi.org/10.1111/j.1551-2916.2011.04448.x>. <https://doi.org/https://doi.org/10.1111/j.1551-2916.2011.04448.x>
- [17] N.L. Ahlborg and D. Zhu, *Surface and Coatings Technology*, Calcium-magnesium aluminosilicate (CMAS) reactions and degradation mechanisms of advanced environmental barrier coatings 237, 79-87 (2013). <https://doi.org/https://doi.org/10.1016/j.surfcoat.2013.08.036>
- [18] K.M. Grant, S. Krämer, G.G.E. Seward and C.G. Levi, *Journal of the American Ceramic Society*, Calcium-Magnesium Alumino-Silicate Interaction with Yttrium Monosilicate Environmental Barrier Coatings 93, 3504-3511 (2010, <https://doi.org/10.1111/j.1551-2916.2010.03916.x>). <https://doi.org/https://doi.org/10.1111/j.1551-2916.2010.03916.x>
- [19] D.L. Poerschke and C.G. Levi, *Journal of the European Ceramic Society*, Effects of cation substitution and temperature on the interaction between thermal barrier oxides and molten CMAS 35, 681-691 (2015). <https://doi.org/https://doi.org/10.1016/j.jeurceramsoc.2014.09.006>
- [20] H. Zhao, B.T. Richards, C.G. Levi and H.N.G. Wadley, *Surface and Coatings Technology*, Molten silicate reactions with plasma sprayed ytterbium silicate coatings 288, 151-162 (2016). <https://doi.org/https://doi.org/10.1016/j.surfcoat.2015.12.053>
- [21] D.L. Poerschke, T.L. Barth, O. Fabrichnaya and C.G. Levi, *Journal of the European Ceramic Society*, Phase equilibria and crystal chemistry in the calcia-silica-yttria system 36, 1743-1754 (2016). <https://doi.org/https://doi.org/10.1016/j.jeurceramsoc.2016.01.046>

- [22] J.L. Stokes, B.J. Harder, V.L. Wiesner and D.E. Wolfe, *Journal of the European Ceramic Society*, High-Temperature thermochemical interactions of molten silicates with Yb₂Si₂O₇ and Y₂Si₂O₇ environmental barrier coating materials 39, 5059-5067 (2019). <https://doi.org/https://doi.org/10.1016/j.jeurceramsoc.2019.06.051>
- [23] F. Jiang, L. Cheng and Y. Wang, *Ceramics International*, Hot corrosion of RE₂SiO₅ with different cation substitution under calcium–magnesium–aluminosilicate attack 43, 9019-9023 (2017). <https://doi.org/https://doi.org/10.1016/j.ceramint.2017.04.045>
- [24] Z. Tian, X. Ren, Y. Lei, L. Zheng, W. Geng, J. Zhang and J. Wang, *Journal of the European Ceramic Society*, Corrosion of RE₂Si₂O₇ (RE=Y, Yb, and Lu) environmental barrier coating materials by molten calcium-magnesium-alumino-silicate glass at high temperatures 39, 4245-4254 (2019). <https://doi.org/https://doi.org/10.1016/j.jeurceramsoc.2019.05.036>
- [25] L.R. Turcer, A.R. Krause, H.F. Garces, L. Zhang and N.P. Padture, *Journal of the European Ceramic Society*, Environmental-barrier coating ceramics for resistance against attack by molten calcia-magnesia-aluminosilicate (CMAS) glass: Part II, β-Yb₂Si₂O₇ and β-Sc₂Si₂O₇ 38, 3914-3924 (2018). <https://doi.org/https://doi.org/10.1016/j.jeurceramsoc.2018.03.010>
- [26] F. Stolzenburg, P. Kenesei, J. Almer, K.N. Lee, M.T. Johnson and K.T. Faber, *Acta Materialia*, The influence of calcium–magnesium–aluminosilicate deposits on internal stresses in Yb₂Si₂O₇ multilayer environmental barrier coatings 105, 189-198 (2016). <https://doi.org/https://doi.org/10.1016/j.actamat.2015.12.016>
- [27] A. Abdul-Aziz and R.T. Bhatt, *Journal of Composite Materials*, Modeling of thermal residual stress in environmental barrier coated fiber reinforced ceramic matrix composites 46, 1211-1218 (2011). <https://doi.org/10.1177/0021998311414950>
- [28] A.R. Krause, H.F. Garces, B.S. Senturk and N.P. Padture, *Journal of the American Ceramic Society*, 2ZrO₂·Y₂O₃ Thermal Barrier Coatings Resistant to Degradation by Molten CMAS: Part II, Interactions with Sand and Fly Ash 97, 3950-3957 (2014). <https://doi.org/https://doi.org/10.1111/jace.13209>
- [29] J.M. Drexler, A.L. Ortiz and N.P. Padture, *Acta Materialia*, Composition effects of thermal barrier coating ceramics on their interaction with molten Ca–Mg–Al–silicate (CMAS) glass 60, 5437-5447 (2012). <https://doi.org/https://doi.org/10.1016/j.actamat.2012.06.053>
- [30] N.K. Eils, P. Mechnich and W. Braue, *Journal of the American Ceramic Society*, Effect of CMAS Deposits on MOCVD Coatings in the System Y₂O₃–ZrO₂: Phase Relationships 96, 3333-3340 (2013). <https://doi.org/https://doi.org/10.1111/jace.12502>
- [31] J.J. Gomez Chavez, R. Naraparaju, P. Mechnich, K. Kelm, U. Schulz and C.V. Ramana, *Journal of Materials Science & Technology*, Effects of yttria content on the CMAS infiltration resistance of yttria stabilized thermal barrier coatings system 43, 74-83 (2020). <https://doi.org/https://doi.org/10.1016/j.jmst.2019.09.039>
- [32] J.J.G. Chavez, R. Naraparaju, C. Mikulla, P. Mechnich, K. Kelm, C.V. Ramana and U. Schulz, *Corrosion Science*, Comparative study of EB-PVD gadolinium-zirconate and yttria-rich zirconia coatings performance against Fe-containing calcium-magnesium-aluminosilicate (CMAS) infiltration 190, 109660 (2021). <https://doi.org/https://doi.org/10.1016/j.corsci.2021.109660>
- [33] R. Naraparaju, J.J. Gomez Chavez, U. Schulz and C.V. Ramana, *Acta Materialia*, Interaction and infiltration behavior of Eyjafjallajökull, Sakurajima volcanic ashes and a synthetic CMAS containing FeO with/in EB-PVD ZrO₂-65 wt% Y₂O₃ coating at high temperature 136, 164-180 (2017). <https://doi.org/https://doi.org/10.1016/j.actamat.2017.06.055>
- [34] P. Mechnich, *43rd International conference and exposition on advanced ceramics and composites*, Complex Melting Behavior of Si-lean, Fe-Ti-CMAS and its effects on the Recession of EB-PVD Gadolinium-Zirconate TBC (2019).
- [35] R. Naraparaju, CMAS-Resistente Schutzschicht DE 10 2017 119 387 A1 2019.02.28 (2017).
- [36] R. Naraparaju, CMAS resistant Protective layer US2019/0062898 (2019).
- [37] M.A. Rivera-Gil, J.J. Gomez-Chavez, C.V. Ramana, R. Naraparaju, U. Schulz and J. Muñoz-Saldaña, *Surface and Coatings Technology*, High temperature interaction of volcanic ashes with 7YSZ TBC's produced by APS: Infiltration behavior and phase stability 378, 124915 (2019). <https://doi.org/https://doi.org/10.1016/j.surfcoat.2019.124915>
- [38] C.Y. Guijosa-Garcia, M.A. Rivera-Gil, C.V. Ramana, R. Naraparaju, U. Schulz and J. Muñoz-Saldaña, *JOM*, Reaction Products from High Temperature Treatments of (LaxGd_{1-x})₂Zr₂O₇

- System and Volcanic Ash Powder Mixtures 74, 2791-2808 (2022).
<https://doi.org/10.1007/s11837-022-05302-3>
- [39] S. Krämer, J. Yang, C.G. Levi and C.A. Johnson, *Journal of the American Ceramic Society*, Thermochemical Interaction of Thermal Barrier Coatings with Molten CaO–MgO–Al₂O₃–SiO₂ (CMAS) Deposits 89, 3167-3175 (2006, <https://doi.org/10.1111/j.1551-2916.2006.01209.x>). <https://doi.org/https://doi.org/10.1111/j.1551-2916.2006.01209.x>
- [40] R. Anton, V. Leisner, P. Watermeyer, M. Engstler and U. Schulz, *Acta Materialia*, Hafnia-doped silicon bond coats manufactured by PVD for SiC/SiC CMCs 183, 471-483 (2020).
<https://doi.org/https://doi.org/10.1016/j.actamat.2019.10.050>
- [41] P. Mechnich, *Surface and Coatings Technology*, Y₂SiO₅ coatings fabricated by RF magnetron sputtering 237, 88-94 (2013). <https://doi.org/https://doi.org/10.1016/j.surfcoat.2013.08.015>
- [42] V. Leisner, *LINCET I Symposium*, Development of EBCs for SiC/SiC CMCs Employing PVD Technologies (2017).
- [43] R. Anton, V. Leisner, N. Laska and U. Schulz, *Coatings*, Reactive Sputtered Ytterbium Silicate Environmental Barrier Coatings for Protection of Mo-Si-Based Alloys 12, 1086 (2022).
- [44] H.J. Seifert, S. Wagner, O. Fabrichnaya, H.L. Lukas, F. Aldinger, T. Ullmann, M. Schmücker and H. Schneider, *Journal of the American Ceramic Society*, Yttrium Silicate Coatings on Chemical Vapor Deposition-SiC-Precoated C/C–SiC: Thermodynamic Assessment and High-Temperature Investigation 88, 424-430 (2005). <https://doi.org/https://doi.org/10.1111/j.1551-2916.2005.00077.x>
- [45] R. Przeliorz, M. Goral, M. Grzegorz and L. Swadzba, *Journal of Achievements in Materials and Manufacturing Engineering*, The relationship between specific heat capacity and oxidation resistance of TiAl alloys 21 (2007).
- [46] J. Parmentier, K. Liddell, D.P. Thompson, H. Lemerrier, N. Schneider, S. Hampshire, P.R. Bodart and R.K. Harris, *Solid State Sciences*, Influence of iron on the synthesis and stability of yttrium silicate apatite 3, 495-502 (2001). [https://doi.org/https://doi.org/10.1016/S1293-2558\(01\)01151-7](https://doi.org/https://doi.org/10.1016/S1293-2558(01)01151-7)
- [47] R.D. Shannon, *Acta Crystallographica Section A*, Revised effective ionic radii and systematic studies of interatomic distances in halides and chalcogenides 32, 751-767 (1976).
<https://doi.org/https://doi.org/10.1107/S0567739476001551>
- [48] S.B. Anantharaman, V.B. Rajkumar, S. Raghunandan, K.C. Hari Kumar, R.S. Kumar and A.S. Gandhi, *Journal of the European Ceramic Society*, Role of thermodynamic miscibility gaps in phase selection in sol-gel synthesis of yttrium silicates 37, 5001-5007 (2017).
<https://doi.org/https://doi.org/10.1016/j.jeurceramsoc.2017.06.040>